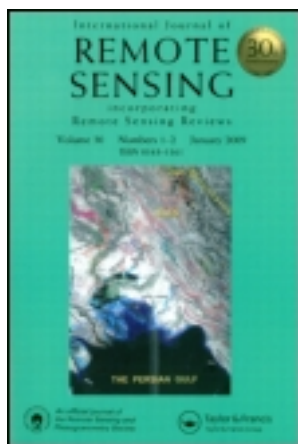


This article was downloaded by: [USGS Libraries Program]

On: 25 June 2012, At: 08:58

Publisher: Taylor & Francis

Informa Ltd Registered in England and Wales Registered Number: 1072954 Registered office: Mortimer House, 37-41 Mortimer Street, London W1T 3JH, UK



International Journal of Remote Sensing

Publication details, including instructions for authors and subscription information:

<http://www.tandfonline.com/loi/tres20>

Simulation of time-series surface deformation to validate a multi-interferogram InSAR processing technique

Chang-Wook Lee ^a, Zhong Lu ^b & Hyung-Sup Jung ^c

^a ASRC Research and Technology Solutions, US Geological Survey, Cascades Volcano Observatory, Vancouver, WA, 98683, USA

^b US Geological Survey, Cascades Volcano Observatory, Vancouver, WA, 98683, USA

^c Department of Geoinformatics, University of Seoul, Seoul, 130-743, Korea

Available online: 22 Jun 2012

To cite this article: Chang-Wook Lee, Zhong Lu & Hyung-Sup Jung (2012): Simulation of time-series surface deformation to validate a multi-interferogram InSAR processing technique, International Journal of Remote Sensing, 33:22, 7075-7087

To link to this article: <http://dx.doi.org/10.1080/01431161.2012.700137>

PLEASE SCROLL DOWN FOR ARTICLE

Full terms and conditions of use: <http://www.tandfonline.com/page/terms-and-conditions>

This article may be used for research, teaching, and private study purposes. Any substantial or systematic reproduction, redistribution, reselling, loan, sub-licensing, systematic supply, or distribution in any form to anyone is expressly forbidden.

The publisher does not give any warranty express or implied or make any representation that the contents will be complete or accurate or up to date. The accuracy of any instructions, formulae, and drug doses should be independently verified with primary sources. The publisher shall not be liable for any loss, actions, claims, proceedings,

demand, or costs or damages whatsoever or howsoever caused arising directly or indirectly in connection with or arising out of the use of this material.

Simulation of time-series surface deformation to validate a multi-interferogram InSAR processing technique

CHANG-WOOK LEE[†], ZHONG LU[‡] and HYUNG-SUP JUNG^{*§}

[†]ASRC Research and Technology Solutions, US Geological Survey, Cascades Volcano Observatory, Vancouver, WA 98683, USA

[‡]US Geological Survey, Cascades Volcano Observatory, Vancouver, WA 98683, USA

[§]Department of Geoinformatics, University of Seoul, Seoul 130-743, Korea

(Received 3 January 2012; in final form 1 April 2012)

A refined, small baseline subset (SBAS) interferometric synthetic aperture (InSAR) method has been developed to estimate time-series surface deformation through fusion of multi-interferogram processing. Using a synthetic data set that takes into account two time-varying deformation sources, topography-induced errors, atmospheric delay anomalies, orbital errors and temporal decorrelation, all of which are based on realistic ERS-1/ERS-2 SAR image acquisition dates and baseline configuration over the Seguam volcano, Alaska, we assess the accuracy of the refined SBAS technique. Detailed comparison between SBAS-derived products, including time-series deformation maps, atmospheric delays and baseline errors with those of synthetic values, attest the robustness of the refined SBAS technique. The root mean square error of the mean deformation rate between the simulated and SBAS-retrieved is about $0.66 \text{ mm year}^{-1}$. Thus, the measurement accuracy of the refined SBAS method would be around 1 mm year^{-1} .

1. Introduction

The small baseline subset (SBAS) interferometric synthetic aperture (InSAR) technique (Berardino *et al.* 2002) has been developed to map time-series ground surface deformation using a multi-interferogram processing approach. To achieve time-series deformation measurement from multiple interferograms, the SBAS algorithm first estimates the mean deformation rate and the topographic error. The atmospheric artefacts are mitigated through temporal high-pass and spatial low-pass filtering of interferograms after the mean deformation rates have been removed. Because the interferograms are not adjacently linked (i.e. there may be temporal overlaps or underlaps between them), SBAS InSAR uses the singular value decomposition (SVD) approach based on a minimum-norm criterion of the deformation rate to derive time-series deformation measurements.

Although the SBAS algorithm (Berardino *et al.* 2002) is very effective in measuring time-series deformation, the suppression of errors caused by temporal decorrelation and other noise effects is not properly addressed. Linear deformation rates estimated using interferograms having unwrapping errors often lead to misestimates of the actual

*Corresponding author. Email: hsjung@uos.ac.kr

deformation history. Estimates of atmospheric artefacts and topographic errors based on the assumption of linear deformation rate during the periods spanned by individual interferograms can further detract from the retrieval of accurate time-series deformation measurements. Moreover, the atmospheric artefact and orbital error at the reference point (a pixel location used to reference interferogram phase values at other pixels) have not been properly addressed, which can affect the deformation measurements.

A refined SBAS InSAR algorithm (Lee *et al.* 2011) has been developed to improve estimates of time-series deformation through iterative processing. With this algorithm, phase unwrapping errors can be corrected by distinguishing between high-quality (HQ) images in which no unwrapping errors could be found and low-quality (LQ) ones where phase jumps due to unwrapping errors are possible. Estimations of atmospheric artefacts, topographic errors and time-series deformation measurements are refined through an iteration procedure. The temporal noise is further mitigated by the finite-difference smoothing approach (Schmidt and Burgmann 2003, Lee *et al.* 2011).

Furthermore, possible phase bias at the reference point due to orbital and atmospheric phase artefacts is evaluated. In this study, we propose to systematically assess the accuracy of the refined SBAS technique using synthetic data sets (table 1) that are based on realistic ERS-1/ERS-2 SAR image acquisitions over the Seguam volcano, Alaska, where time-variant ground surface deformation has been observed (Lee *et al.* 2012).

2. Data processing

Based on ERS-1/ERS-2 Track 201 SAR acquisitions over the Seguam volcano, Alaska, we generate 48 synthetic interferograms that maintain good coherence during 1993–2007 (table 1). These interferograms have perpendicular baselines of less than 300 m and temporal separations of less than 5 years. Each of the synthetic interferograms contains ground surface deformation, atmospheric contribution, orbit error, topographic error, temporal decorrelation and noise:

$$\Delta\varphi(x, r) \approx \frac{4\pi}{\lambda} \left\{ \Delta d(x, r) + \frac{B_{\perp}}{r \sin \theta} \Delta z_{\text{topo}}(x, r) \right\} + \Delta\varphi_{\text{atmo}}(x, r) + \Delta\varphi_{\text{orbit}}(x, r) + \Delta\varphi_{\text{temp}}(x, r) + \Delta\varphi_n(x, r), \quad (1)$$

where x and r are the azimuth and slant range pixel coordinates, respectively, λ is the radar wavelength, B_{\perp} is the perpendicular baseline, θ is the SAR look angle, Δd is the surface displacement in the radar look direction, Δz_{topo} is the topographic error, $\Delta\varphi_{\text{atmo}}$ is the atmospheric phase delay artefact, $\Delta\varphi_{\text{orbit}}$ is the baseline error, $\Delta\varphi_{\text{temp}}$ is the temporal decorrelation and $\Delta\varphi_n$ is the phase due to other noise sources. The phase components due to deformation, atmospheric delay, orbit error, digital elevation model (DEM) error and temporal decorrelation (Zebker and Villasenor 1992) were simulated, separated and then combined to produce the synthetic interferograms for SBAS processing.

2.1 Simulation of surface deformation

Seguam Island comprises the remnants of two late Quaternary calderas, one in the western part of the island and the other in the eastern part. The western caldera

Table 1. Characteristics of ERS-1 and ERS-2 data used in this study.

Number	Mission	Orbit	Date	Baseline (m)
1	ERS-1	9865	4 June 1993	0
2	ERS-1	10 366	9 July 1993	-57.83
3	ERS-1	10 867	13 August 1993	823.70
4	ERS-1	11 368	17 September 1993	1394.73
5	ERS-1	11 869	22 October 1993	1661.45
6	ERS-1	20 229	28 May 1995	731.54
7	ERS-1	21 732	10 September 1995	143.61
8	ERS-2	12 580	15 September 1997	977.27
9	ERS-2	13 081	20 October 1997	953.17
10	ERS-2	18 091	5 October 1998	1430.36
11	ERS-2	18 592	9 November 1998	1768.03
12	ERS-2	22 099	12 July 1999	1034.40
13	ERS-2	22 600	16 August 1999	2100.08
14	ERS-2	23 101	20 September 1999	980.55
15	ERS-2	28 111	4 September 2000	998.18
16	ERS-2	29 113	13 November 2000	919.62
17	ERS-2	33 121	20 August 2001	901.64
18	ERS-2	38 131	5 August 2002	128.19
19	ERS-2	38 632	9 September 2002	1368.99
20	ERS-2	39 133	14 October 2002	1251.34
21	ERS-2	42 640	16 June 2003	470.41
22	ERS-2	43 141	21 July 2003	635.77
23	ERS-2	44 143	29 September 2003	1756.68
24	ERS-2	44 644	3 November 2003	1110.21
25	ERS-2	47 650	31 May 2004	444.77
26	ERS-2	49 153	13 September 2004	832.66
27	ERS-2	49 654	18 October 2004	1685.89
28	ERS-2	53 662	25 July 2005	1023.48
29	ERS-2	58 171	5 June 2006	627.30
30	ERS-2	58 672	10 July 2006	974.32
31	ERS-2	59 674	18 September 2006	993.77
32	ERS-2	60 175	23 October 2006	1387.64
33	ERS-2	63 682	25 June 2007	1127.16
34	ERS-2	64 183	30 July 2007	1740.73

subsided at a constant rate of $\sim 1.5 \text{ cm year}^{-1}$ throughout the study period, while the eastern caldera experienced alternating periods of subsidence and uplift: $\sim 1.5 \text{ cm year}^{-1}$ subsidence during June 1993–July 1999 (stage 1), $\sim 2.5 \text{ cm year}^{-1}$ uplift during July 1999–November 2000 (stage 2), $\sim 1.5 \text{ cm year}^{-1}$ subsidence during November 2000–July 2005 (stage 3) and $\sim 2 \text{ cm year}^{-1}$ uplift during July 2005–2007 (stage 4) (Lee *et al.* 2012). Source modelling indicates a deflationary source $\sim 2 \text{ km}$ below sea level (BSL) beneath the western caldera and two sources beneath the eastern caldera: an inflationary source $\sim 4 \text{ km}$ BSL and a deflationary source $\sim 2 \text{ km}$ BSL (Lee *et al.* 2012).

For point-pressure (Mogi) (Mogi 1958, Lu *et al.* 2002, 2003, 2005) source, a component of deformation vector (u_i) and the displacement at the free surface ($x_3 = 0$) take the form

$$u_i(x_1 - x'_1, x_2 - x'_2, -x_3) = C \frac{x_i - x'_i}{|R^3|}, \quad (2)$$

where x'_i is a source location, C is a combination of material properties and source strength and R is the distance from the source to the surface location. Line-of-sight (LOS) deformation measured by InSAR can be obtained by $u_i l_i$, where l_i ($i = 1, 2, 3$) is the LOS vector defined by the radar incidence angle and the satellite track angle. Synthetic deformation interferograms are produced using Mogi sources based on parameters from the time-series InSAR analysis of Segoum during 1993 and 2007 (Lee *et al.* 2012), and the deformation signals are reduced by 60% to assess the accuracy of the refined SBAS technique effectively. Two examples of deformation interferograms are shown in figures 1(a) and (g).

2.2 Simulation of topographic error

In InSAR, topographic error is nearly linearly related to the InSAR phase error as follows:

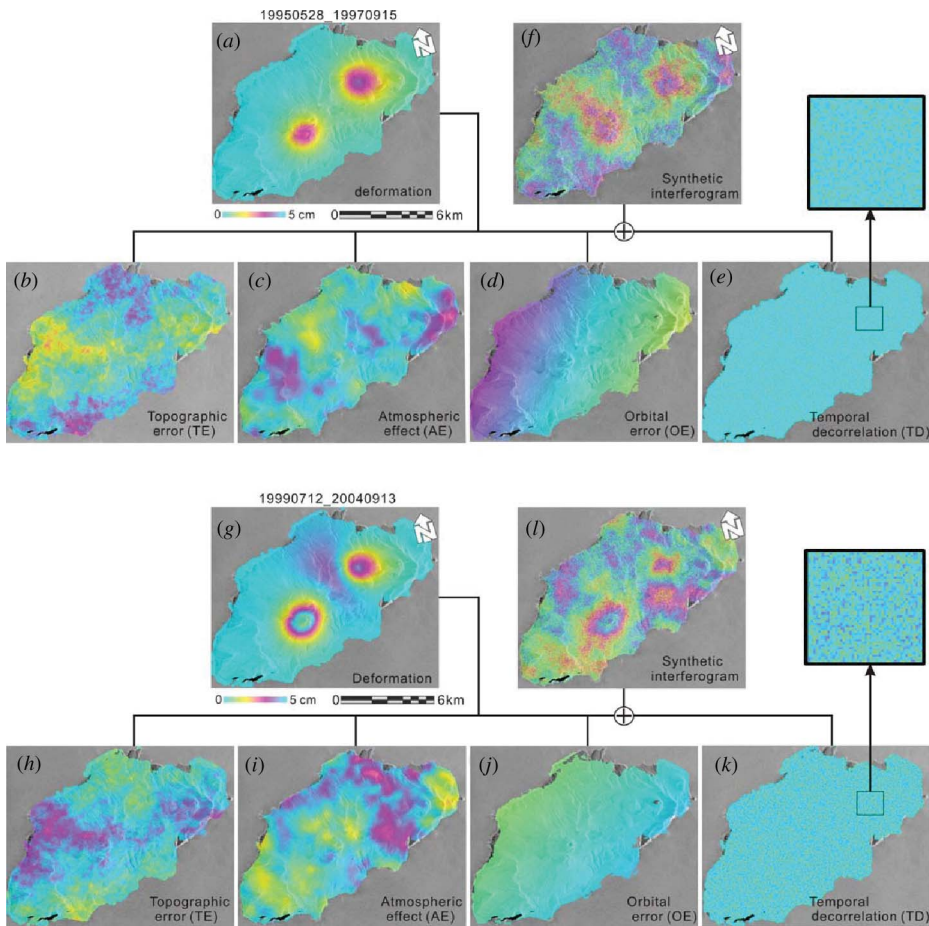


Figure 1. Two examples of (a, g) simulated deformation-only interferograms, (b, h) simulated topographic residual errors of interferograms, (c, i) simulated atmospheric artefacts, (d, j) simulated orbital errors, (e, k) simulated temporal decorrelation noise and (f, l) summation of simulated deformation and all error components. The phase images have been plotted on an SAR amplitude map.

$$\Delta\phi_{\text{topo}}(x, r) = \frac{4\pi B_{\perp}}{\lambda r \sin \theta} \Delta z, \quad (3)$$

where $\Delta\phi_{\text{topo}}$ is the phase error due to a topography error Δz for an interferogram with a perpendicular baseline B_{\perp} . We simulate maps of topographic errors using isotropic two-dimensional fractal surfaces (Ramon 2005). We allow for topographic errors ranging from -20 to 20 m, which are about the noise level for Shuttle Radar Topographic Mission (SRTM) DEM. Figures 1(b) and (h) show two examples of topography-induced phase error maps used in this study.

2.3 Simulation of atmospheric artefact

An atmospheric artefact is the time delay between the transmitted and reflected radar signals by the variation of water vapours in the troposphere (Zebker *et al.* 1997). This artefact is one of the prominent error sources in InSAR deformation mapping because it causes a severe phase distortion in a SAR image. We simulate tropospheric phase delay (Doin *et al.* 2009) by assuming that this signal has homogeneous atmospheric conditions and radially symmetric structures within the interferograms (Ramon 2005). We use the one-dimensional covariance function proposed by Biggs *et al.* (2007) to simulate the atmospheric effects over the Segum volcano:

$$C_{ij} = \sigma^2 e^{(-d_{ij}/\alpha)}, \quad (4)$$

where C_{ij} and d_{ij} are the covariance of atmospheric artefact and the distance between pixels i and j , respectively, σ is the variance and α is the wavelength of the atmospheric delay (Biggs *et al.* 2007). Based on atmospheric delay observations on interferograms with short time separations (when deformation is negligible), we estimate the typical ranges for σ and α , based on which we allow σ to vary from 15 to 5 mm and α to vary from 15 to 5 km to simulate the atmospheric delay. Figures 1(c) and (i) show two examples of atmospheric delay phases. Simulated atmospheric interferograms are superimposed on the simulated deformation signal.

2.4 Simulation of orbital error

A significant error source in InSAR deformation mapping is the baseline uncertainty due to inaccurate determination of SAR antenna positions. For most radar satellites, the refined precision orbit data should be used for InSAR processing. Even for some satellites where precise restitute vectors are available, baseline errors in interferograms can often be present. For example, the precision restitute vectors for ERS-1, ERS-2 (Kohlhase *et al.* 2003) and the Environmental Satellite (ENVISAT) (Otten and Boonkamp 2003) have accuracies of about 7 cm in radial and 18 cm in the across-track directions with the Delft Gravity Model (DGM)-E04 and Geo Forschungs Zentrum (GFZ) PGM055 (Scharroo and Visser 1998). The interferometric baseline error of ERS-1/2 can be about 27 cm, which is calculated to be $\sqrt{2}$ times the satellite's position error (about 19 cm). Given the system parameters of ERS-1/ERS-2, the phase error difference from near to far ranges is approximately 2.3π rad, which corresponds to about 3.3 cm of apparent deformation. In this article, we model the interferogram phase error due to baseline error using a first-order polynomial:

$$\Delta\varphi_{\text{orbit}}(x, r) = ax + br + c, \quad (5)$$

where a and b are gradient parameters in range and azimuth coordinates r and x , and c is the offset parameter. We allow for a maximum phase distortion of about 4 cm within an InSAR image according to the phase distortion of about 3.3 cm by the typical baseline error of ERS system. The random parameters of a , b and c in equation (5) are estimated for each interferogram and used for this orbital error simulation. Two examples of orbital error components are shown in figures 1(d) and (j).

2.5 Simulation of temporal decorrelation

The temporal decorrelation results from physical changes in the terrain surface such as vegetation growth, soil moisture and other environmental factors between two SAR image acquisitions (Santoro *et al.* 2010). Calculation of temporal decorrelation requires very complicated functions since it relies on subtle changes to scatterers. We explore 48 coherence maps extracted from real C-band interferograms observed over the Seguam volcano. As seen in figure 2, the time separations of the interferograms range from 280 to 1890 days, and the mean coherence values vary from about 0.88 to about 0.52. From figure 2, we conclude that the temporal correlation (γ_{temp}) decreases exponentially with time:

$$\gamma_{\text{temp}} = \exp(-\beta \Delta T), \quad (6)$$

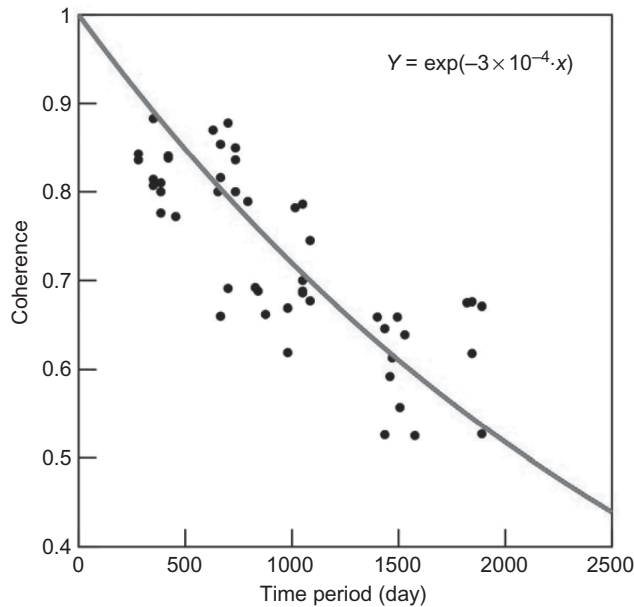


Figure 2. Temporal decorrelation model (curve) using coherence measurements (solid circles) over the Seguam volcano, Alaska.

where ΔT shows the time period according to each interferogram and β is a parameter characterizing temporal decay of InSAR coherence. The InSAR phase variance due to temporal decorrelation can then be approximated by (Rodríguez and Martin 1992)

$$\sigma_{\phi}^2 = \frac{1 - \gamma_{\text{temp}}^2}{2N\gamma_{\text{temp}}^2}, \quad (7)$$

where N is the independent number of looks used to generate the interferogram. We simplify the simulation by estimating β from realistic coherence maps (see figure 2) and adding random phases, which have time-variant standard deviations estimated from equations (6) and (7), into synthetic interferograms. Two examples of temporal decorrelation images are shown in figures 1(e) and (k).

3. Validation of SBAS DInSAR processing using simulated data sets

We now have simulated 48 interferograms that include ground surface deformation, atmospheric delays, orbital errors, DEM-induced errors and decorrelation noise. The respective errors have been simulated using typical values obtained from normal atmospheric conditions, the orbit accuracy of ERS-1/ERS-2 SAR, the height accuracy of SRTM DEM and coherence variation of real interferograms. We apply SBAS processing on this set of simulated interferograms. The refined SBAS processing flow is shown in figure 3. The retrieved surface deformation images from the SBAS processing are shown in figures 4(d) and (i). The difference between the simulated interferograms (figures 4(b) and (g)) and the retrieved deformation interferograms (figures 4(d) and (i)) includes primarily the atmospheric artefacts, orbit errors and decorrelation noise (figures 4(c) and (h)). We can see that the SBAS technique is an efficient way to filter out atmospheric artefacts and orbit errors by using temporally high-pass and spatially low-pass filtering of multi-temporal interferograms. Multi-temporal InSAR methods including the refined SBAS might fail to extract the deformation component from multi-temporal interferograms if the error contribution effects to interferograms are much larger than deformation signals.

The SBAS-retrieved deformation images (figures 4(d) and (i)) are compared with the ‘truth’ deformation images (figures 4(a) and (f)), and the results are shown in figures 4(e) and (j). As seen in figures 4(e) and (j), the means of the residual images are 0.56 and 0.34 mm, respectively, and the standard deviations of the residual images are 0.44 and 0.77 mm, respectively. We also compare the mean deformation rate during 1993–2007 between the simulated and the SBAS-retrieved (figure 5). The mean and standard deviation of the difference image are 0.61 and 0.25 mm year⁻¹, respectively, and the root mean square error (RMSE) is about 0.66 mm year⁻¹ (figure 5(c)).

One of the important outputs of SBAS processing is the deformation at individual epoch. Figure 6 shows time-series deformation at two locations over the western caldera and eastern caldera. The SBAS-retrieved deformation patterns agree well with the simulated deformation, suggesting the effectiveness of the SBAS processing technique. In particular, SBAS processing produces time-variant deformation patterns that fit well with the ‘truth’ data. On the western caldera point, the difference between SBAS-derived and ‘truth’ data has a mean value of 0.2 mm and a standard deviation of 1.4 mm. On the eastern caldera point, the difference between the retrieved

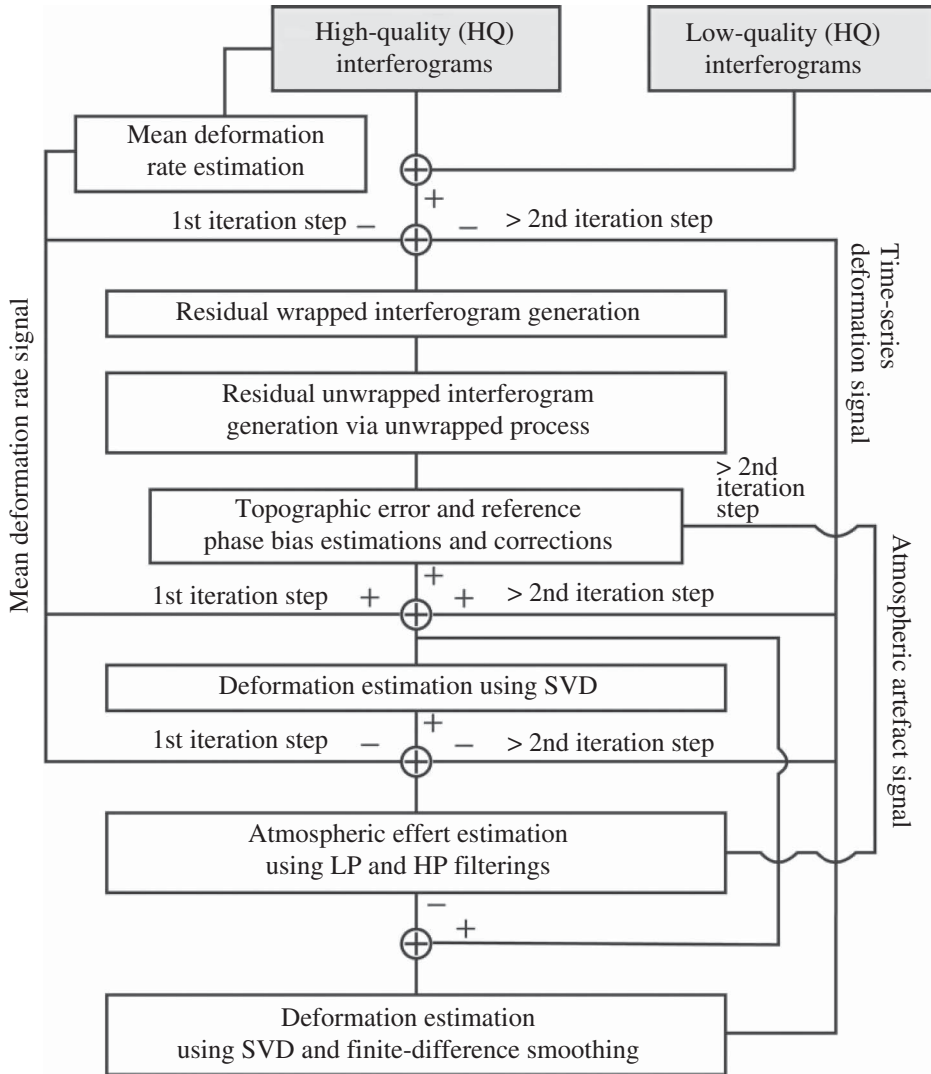


Figure 3. Block diagram of our SBAS InSAR processing algorithm [2].

and the ‘truth’ is slightly worse than that over the western caldera: the mean reaches 0.9 mm and the standard deviation is 1.6 mm (figure 6(b)). These differences are likely due to the differences in their deformation characteristics between the western caldera and the eastern caldera. The deformation over the western caldera is stable, while the deformation over the eastern caldera fluctuates with time. Figure 7 shows the SBAS-derived and ‘truth’ deformation along profile A–A’. The absolute difference between the two deformation profiles is less than 1.1 mm year⁻¹ and the standard deviation is 0.2 mm year⁻¹. The scatter plot between the SBAS-retrieved deformation rates and the ‘truth’ is shown in figure 8. The coefficient of determination reaches $R^2 = 0.94$, suggesting that the SBAS can retrieve the time-variant deformation very well.

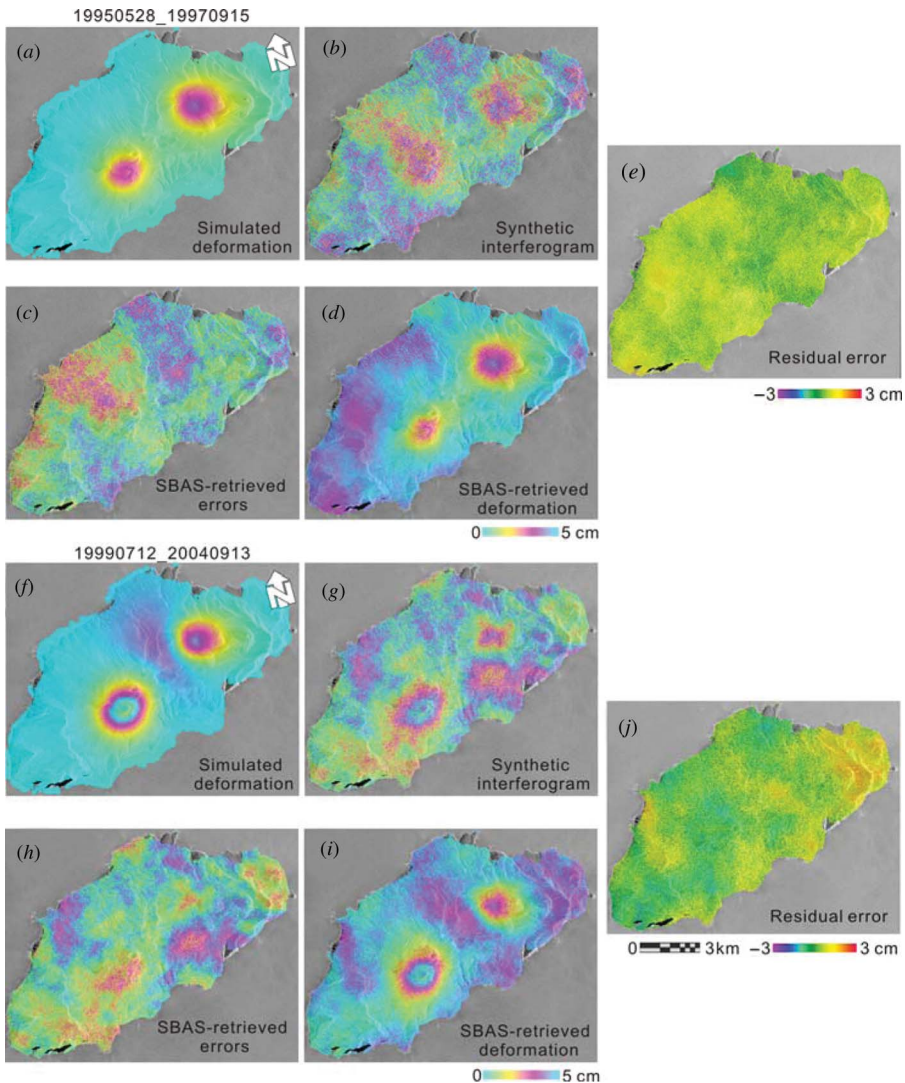


Figure 4. Deformation and error images retrieved from SBAS processing of multi-temporal simulated interferograms with error components. Two examples of (a, f) deformation-only interferograms, (b, g) synthetic interferograms that are generated by sum of deformation and all error components including topography, atmosphere and baseline artefacts and decorrelation noise, (c, h) retrieved error images after SBAS processing, (d, i) retrieved deformation images through SBAS processing of multi-temporal interferograms and (e, j) difference images between the simulated deformation and SBAS-derived deformation maps.

4. Conclusions

Our InSAR SBAS method takes into account the atmospheric delay artefacts and DEM errors, uses an iterative approach to correct phase unwrapping errors and includes additional temporal smoothing to suppress atmospheric delay anomalies. We validate our SBAS processing method using simulated deformation observations.

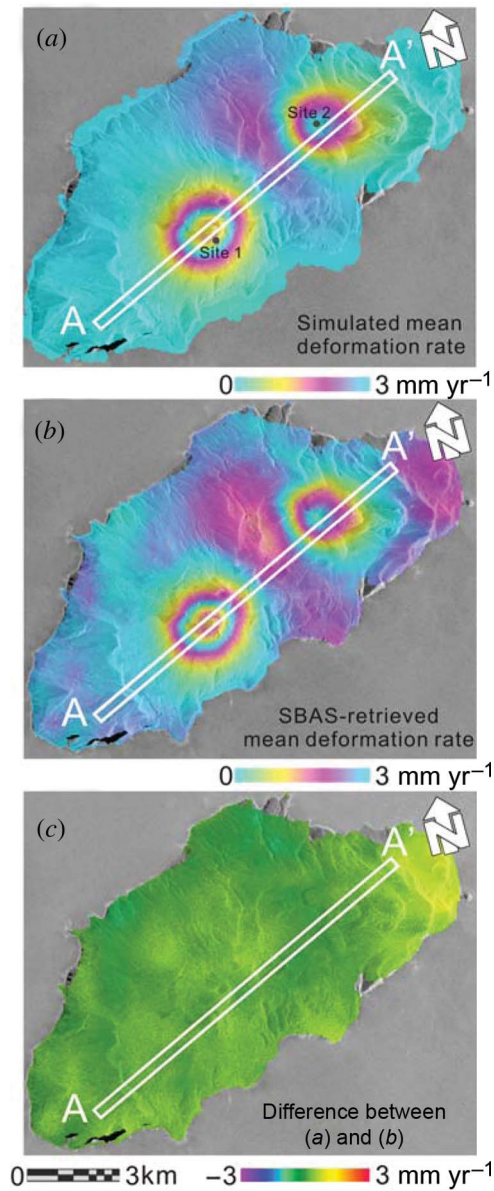


Figure 5. Mean LOS velocity map from simulated deformation interferograms between June 1993 and July 2007. (b) Mean LOS velocity map derived from SBAS processing. (c) Difference interferogram between (a) and (b).

The simulated InSAR images contain time-variant deformation due to two different deformation sources, atmospheric delay anomalies, orbital errors, DEM errors and decorrelation errors. The simulated InSAR observations are also based on the realistic SAR image acquisition time and baseline configuration from ERS-1/ERS-2 Track 201 over the Segoum volcano, western Alaska. A comparison between the retrieved ground surface deformation and ‘truth’ deformation confirms the effectiveness of this

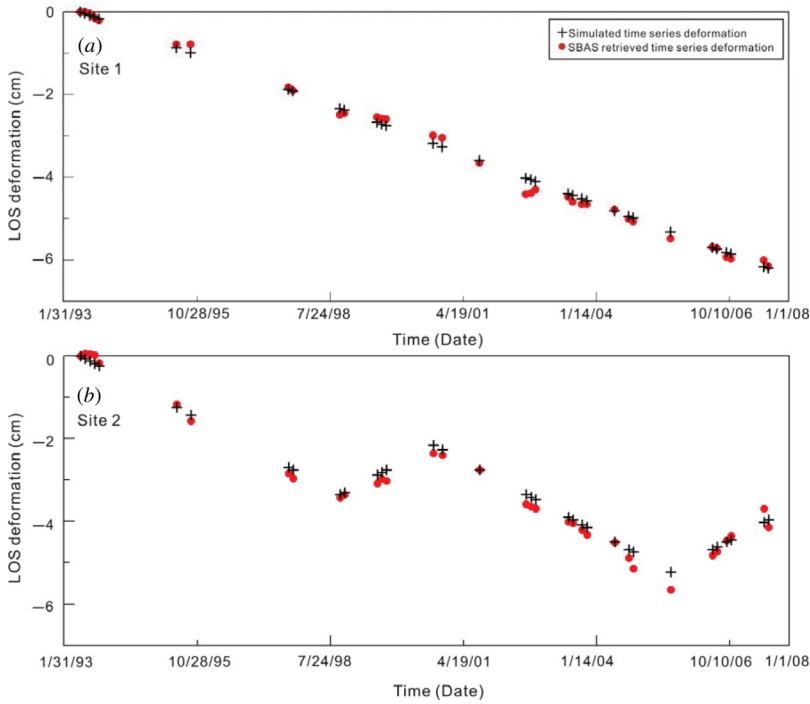


Figure 6. Simulated and SBAS-retrieved LOS time-series deformation at two locations (sites 1 and 2 in figure 5). Crosses represent simulated time-series deformation and circles represent SBAS-derived time-series deformation.

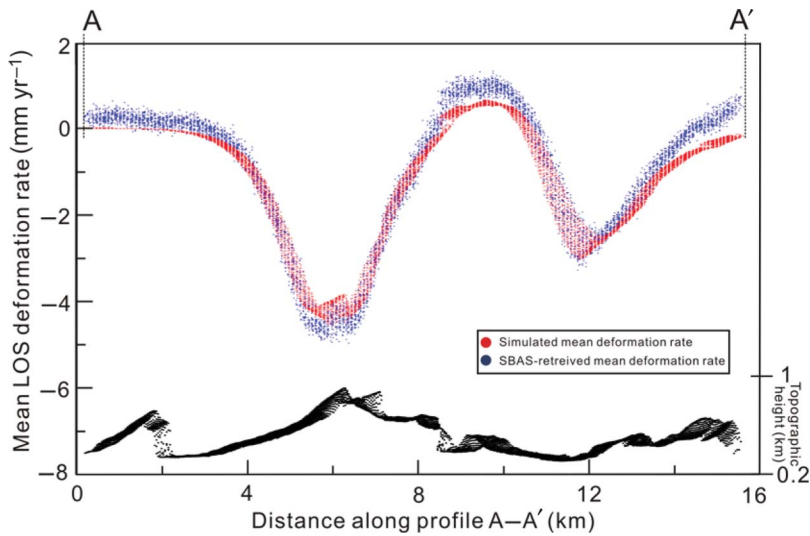


Figure 7. (Top plot) Simulated and SBAS-derived mean LOS velocities over profile A-A' from figure 5. (Bottom plot) Topographic height over profile A-A'.

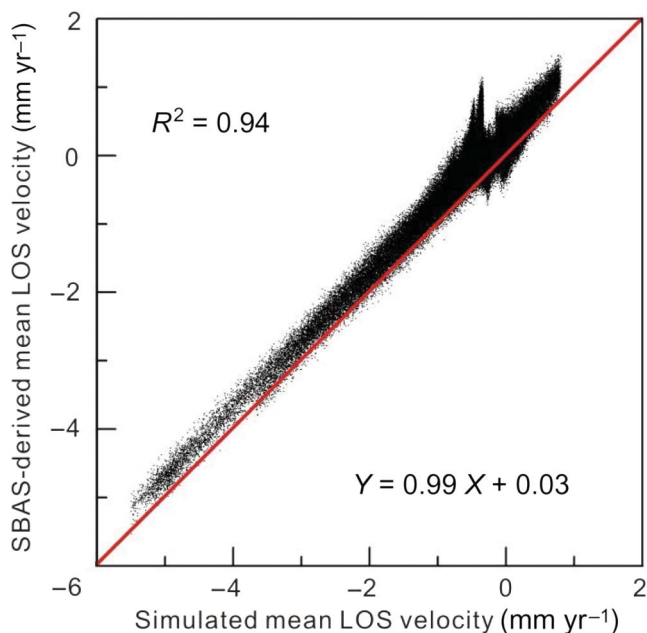


Figure 8. Scattergrams between simulated time-series and SBAS-derived time-series deformation.

SBAS algorithm. We have shown that our SBAS processing can remove and suppress most of the atmospheric delay artefacts and orbital errors. The retrieved deformation rate is less than a few millimetres per year from the ‘truth’ data. Refined SBAS time-series analysis has 0.2–0.9 mm difference from the ‘truth’ data and an RMS error of 0.66 mm year⁻¹. We conclude that our algorithm is effective in extracting time-variant ground surface deformation and various error components. Therefore, the refined SBAS technique has about 1 mm year⁻¹ precision to estimate time-series as well as spatial-domain deformation from multi-temporal interferograms.

Acknowledgements

This research was supported by the NASA Earth Surface and Interior Program (2005/0021), the USGS Volcano Hazards Program and the Korea Research Foundation Grant, funded by the Korean Government (MOEHRD) (KRF-2006-511-C00122). Any use of trade, product or firm names is for descriptive purposes only and does not imply endorsement by the US Government.

References

- BERARDINO, P., FORNARO, G., LANARI, R. and SANSOTI, E., 2002, A new algorithm for surface deformation monitoring based on small baseline differential SAR interferograms. *IEEE Transactions on Geoscience and Remote Sensing*, **36**, pp. 2375–2383.
- BIGGS, J., WRIGHT, T., LU, Z. and PARSONS, B., 2007, Multi-interferogram method for measuring interseismic deformation: Denali Fault, Alaska. *Geophysical Journal International*, **170**, pp. 1165–1179.

- DOIN, M.P., LASSERRE, C., PELTZER, G., CAVALIE, O. and DOUBRE, C., 2009, Corrections of stratified tropospheric delays in SAR interferometry: validation with global atmospheric models. *Journal of Applied Geophysics*, **69**, pp. 35–50.
- KOHLHASE, A.O., FEIGL, K.L. and MASSONNET, D., 2003, Applying differential InSAR to orbital dynamics: a new approach for estimating ERS trajectories. *Journal of Geodesy*, **77**, pp. 493–502.
- LEE, C.-W., LU, Z., JUNG, H.-S., WON, J.-S. and DZURISIN, D., 2011, Surface Deformation of Augustine Volcano (Alaska), 1992–2005, From Multiple-Interferogram Processing Using a Refined SBAS InSAR Approach. *USGS Professional Paper*, **1769**, pp. 453–465.
- LEE, C.-W., LU, Z., JUNG, H.-S., WON, J.-S. and DZURISIN, D., 2012, Dynamic deformation of Segouam volcano, Alaska, 1992–2008, from multi-interferogram InSAR processing. *Journal of Volcanology and Geothermal Research*, in review.
- LU, Z., MASTERLARK, T. and DZURISIN, D., 2005, Interferometric synthetic aperture radar study of Okmok volcano, Alaska, 1992–2003: magma supply dynamics and postemplacement lava flow deformation. *Journal of Geophysical Research*, **110**, doi:10.1029/2004JB003148.
- LU, Z., MASTERLARK, T., DZURISIN, D., RYKHUS, R. and WICK, C., 2003, Magma supply dynamics at Westdahl volcano, Alaska, modeled from satellite radar interferometry. *Journal of Geophysical Research*, **108**, doi:10.1029/2002JB002311.
- LU, Z., MASTERLARK, T., POWER, J., DZURISIN, D. and WICK, C., 2002, Subsidence at Kiska volcano, western Aleutians, detected by satellite radar interferometry. *Geophysical Research of Letters*, **29**, doi:10.1029/2002GL014948.
- MOGI, K., 1958, Relations between the eruptions of various volcanoes and the deformations of the ground surfaces around them. *Earthquake Research Institute, University of Tokyo*, **36**, pp. 99–134.
- OTTEN, M. and BOONKAMP, H., 2003, Estimation of the absolute orbit accuracy of Envisat, European space operation centre, Darmstadt. Available online at: <http://nng.esoc.esa.de/envisat/results/campaign.pdf> (accessed 15 January 2012).
- RAMON, H., 2005, InSAR Matlab tool box. Available online at: <http://doris.tudelft.nl/> (accessed 15 January 2012).
- RODRÍGUEZ, E. and MARTIN, J.M., 1992, Theory and design of interferometric synthetic-aperture radars. In *Proceeding of the Institute of Electrical Engineering*, **139**, pp. 147–159.
- SANTORO, M., WEGMULLER, U. and ASKNE, J.I.H., 2010, Signatures of ERS-Envisat interferometric SAR coherence and phase of short vegetation: an analysis in the case of maize fields. *IEEE Transactions on Geoscience and Remote Sensing*, **48**, pp. 1702–1713.
- SCHARROO, R. and VISSER, P., 1998, Precise orbit determination and gravity field improvement for the ERS satellites. *Journal of Geophysical Research*, **103**, pp. 8113–8127.
- SCHMIDT, D. and BURGMANN, R., 2003, Time-dependent land uplift and subsidence in the Santa Clara valley, California, from a large interferometric synthetic aperture radar data set. *Journal of Geophysical Research*, **108**, doi:10.1029/2002JB002267.
- ZEBKER, H., ROSEN, P. and HENSLEY, S., 1997, Atmospheric effects in interferometric synthetic aperture radar surface deformation and topographic maps. *Journal of Geophysical Research*, **102**, pp. 7547–7563.
- ZEBKER, H. and VILLASENOR, J., 1992, Decorrelation in interferometric radar echoes. *IEEE Transactions on Geoscience and Remote Sensing*, **30**, pp. 950–959.